INTERNATIONAL JOURNAL FOR NUMERICAL METHODS IN FLUIDS
Int. J. Numer. Meth. Fluids 2008; **57**:631–651
Published online 14 April 2008 in Wiley InterScience (www.interscience.wiley.com). DOI: 10.1002/fld.1805

Steady flow through a realistic human upper airway geometry

P. Nithiarasu[1,*,†], O. Hassan[1], K. Morgan[1], N. P. Weatherill[1], C. Fielder[2], H. Whittet[2], P. Ebden[2] and K. R. Lewis[3]

[1]*Civil and Computational Engineering Centre, School of Engineering, Swansea University, Swansea SA2 8PP, U.K.*
[2]*Singleton Hospital, Swansea, U.K.*
[3]*School of Medicine, Swansea University, Swansea SA2 8PP, U.K.*

SUMMARY

Air flow through a human upper airway (central part) has been carried out using a realistic geometry. In addition to explaining the anatomy, problems and importance of patient-specific study of human upper airways, this article also presents some qualitative and quantitative simulation results. As expected, the shear and pressure forces are large in the oropharynx and laryngopharynx, where the flow passage is narrow. This clearly indicates that these locations should be the focus of any study aimed at understanding the human upper airway collapse in a patient-specific manner. Copyright © 2008 John Wiley & Sons, Ltd.

Received 31 July 2007; Revised 18 February 2008; Accepted 18 February 2008

KEY WORDS: patient-specific study; biomedical modelling; fluid dynamics; unstructured meshes; finite elements; incompressible flows; bioflows

1. INTRODUCTION

Over the last five years, there has been a significant increase in patient-specific computational modelling of human body-related problems. The definition of patient-specific study varies from group to group. In this article, we assume any study that employs one or more patient-specific data to be a patient-specific study. The majority of such studies on physiological flows have been focused on the understanding of blood flow and related problems [1–14]. This is mainly due to the fact that cardiovascular problems account for the majority of disease-related deaths in

*Correspondence to: P. Nithiarasu, Civil and Computational Engineering Centre, School of Engineering, Swansea University, Swansea SA2 8PP, U.K.
†E-mail: P.Nithiarasu@swansea.ac.uk

Contract/grant sponsor: EPSRC; contract/grant number: EP/D070554

the developed world. However, the basic causes of cardiovascular problems are more widespread than blood flow behaviour. The problems associated with the human airways may include asthma [15], airway stenosis [16], obstructive sleep apnoea [17, 18], throat cancer [19], nasal airway blockage [20] and chronic obstructive pulmonary disease [21]. Untreated, sleep apnoea can lead to pulmonary hypertension and to heart disease. It is, therefore, essential to give more attention to the human respiratory system. Patient-specific studies on human airways are rather limited and some of these studies concentrate on the lower human airways [22–24]. The upper human airways have received limited attention from the patient-specific numerical modelling community, despite the fact that sleep apnoea, throat cancer and nasal airway blockage are becoming more prevalent in developed countries. However, the trend is changing and some recent studies using realistic geometries demonstrate this [25–28].

There are many fundamental studies available on human upper airway fluid dynamics, but majority of them are carried out on a non-realistic geometry [29]. The basic human airway studies have generally concentrated on simplified geometries assuming, for instance, perfectly circular cross sections of the upper airway or circular triple bifurcation geometries [30–32]. Collapsible tubes have also received significant attention in recent years [33, 34]. It is assumed that some of the theory of collapsible tubes may be extended to help the understanding of upper airway closure. Other basic studies include large eddy simulation (LES) of flow in simplified human airways [35]. The majority of applications in the literature concentrate around the topic of particle transport in upper and lower human airways. Studies on this topic include application to spray dynamics and smoke particles [36–46]. In these studies, in addition to a fluid dynamics algorithm, an efficient way of tracking the particles is essential. The particle tracking studies reported the use of a mixture of simplified geometries and real geometries extracted from real human airways. The fluid dynamic studies on realistic upper human airway geometries are both rare and difficult to carry out, although some attempts have been made in the recent past [25–28]. A combination of geometry extracted from a scan and a hypothetical airway tree has been used by Ma and Lutchen [25]. The objective of the reported work was to estimate the lung resistance from the impedance of small airways. A low-resolution scan with 6 mm cuts were used in the above study. Jeong *et al.* [26] used a subject-specific airway model to estimate the forces in the nasal and central airways. They modelled the flow up to trachea and bifurcation was not included in the study. Brouns *et al.* [27] studied the airway stenosis by introducing a constriction in the upper airway. Both Brouns *et al.* [27] and Jayaraju *et al.* [28] used scans to generate the geometry. The latter study was focused on particle transport. It is also important to note that the commercial codes were used in these studies.

It is apparent that the interest in modelling the flow in the human upper airways is growing and employing realistic geometries in the flow calculation is only a recent trend. Although some studies have been reported in the literature, they are specific to a particular aspect of the airway. In this study, we wish to derive specific flow information at a location just below the tongue base. We are also using the in-house characteristic-based split (CBS) code for the first time to solve flow through a realistic human upper airway geometry. This article also provides comparison with experiments for a model upper airway and uses fully unstructured meshes in the calculations. Using the Spalart–Almaras (SA) turbulence model to a realistic human upper airway is also novel in this work.

This article is organized into the following sections. First, we introduce the anatomy of the human upper airways for completeness and also provide details of disorders of the human upper airways. We provide details on airway collapse and vocal cord paralysis. In Section 3, we provide the

DOI: 10.1002/fld

geometrical modelling and meshing of a realistic upper human airway. Section 4 briefly introduces the fluid dynamic equations and in Section 5 we introduce the solution procedure first and then discuss the results. Section 6 outlines some current difficulties associated with patient-specific modelling. Finally, Section 7 draws some conclusions.

2. ANATOMY AND DISORDERS OF THE HUMAN UPPER AIRWAYS

2.1. Anatomy

To understand the need for, and importance of, patient-specific airway simulation, it is necessary to understand the anatomy of the airway and the common effects of disease on airflow. Figure 1 shows a diagram of a vertical cross section (sagittal) of a typical human upper airway. It is usually divided into anatomically distinct sections, based on anatomical, physiological or pathological considerations. We have divided the upper airway into six segments: the nasal cavities, nasopharynx (including the inferior portion or velopharynx), oropharynx, laryngopharynx, larynx and trachea [18]. The nasal cavities extend from the external nares (nostrils) to the posterior choanae, where the two cavities open into the nasopharynx. The lower part of the nasopharynx (velopharynx) lies behind the soft palate and is highly flexible and constantly changes in shape. It is a common site of snoring. The oropharynx extends from soft palate to the level of the tongue base and the laryngopharynx from tongue base to larynx. The larynx is a valve separating the pharynx and the trachea. The trachea (windpipe) extends from the larynx into the chest and lungs. The walls of the upper airway are formed mostly of soft tissues, including over 20 muscle groups, adipose tissue (fat), tonsil tissue and a flexible mucosal lining. The muscles actively constrict and dilate the lumen of the upper airway [47–49]. In the nasal cavities, larynx and trachea, the walls also contain more rigid cartilaginous and bony structures. A large number and wide range of cross-sectional measurements of the airway have been made [18]. The minimum airway size in the awake state

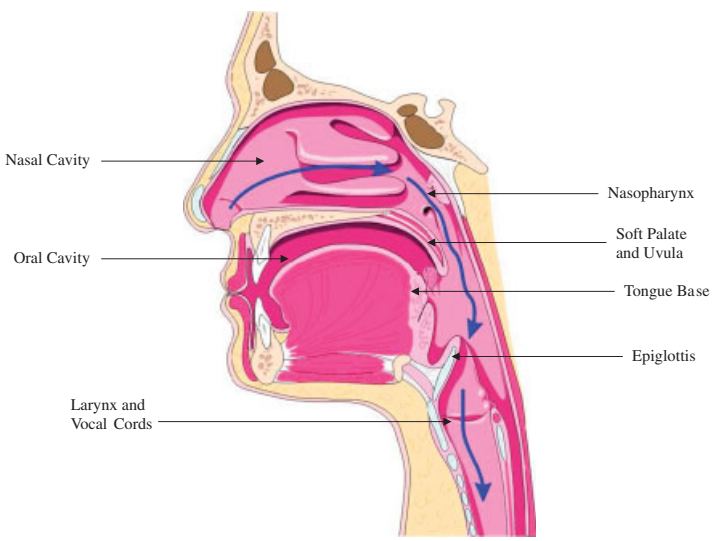

Figure 1. Anatomy of human upper airways.

DOI: 10.1002/fld

occurs at one of the three levels: the anterior nares (nasal valve), the velopharynx (behind the soft palate) and at the junction of larynx and trachea (the subglottis) [50–52]. During sleep the two narrowest portions are at the velopharynx and in the oropharynx at tongue base level. These two sites are of great interest as likely areas of soft tissue collapse of the airway, causing snoring and, most importantly, obstructive sleep apnoea. This makes the oropharynx the site of most interest for modelling. The posterior and lateral walls contain the superior, middle and inferior constrictor muscles, while the anterior wall comprises soft palate and tongue base. The laryngeal and tracheal parts of the airway are much less variable during sleep. However, in the awake state there are significant changes in glottic (laryngeal) area. During quiet breathing the vocal cords open during inspiration, to widen the airway, and close a little during expiration. During phonation the vocal cords are closely approximated with near complete closure of the airway.

2.2. Human airway disorders

The upper airway is susceptible to many diseases. We will focus on two common disorders, each of which predominantly affects one section of the airway.

The first problem of interest is that of vocal cord paralysis. This may be caused by cancer in the chest or neck or the result of surgical trauma to nerves supplying the larynx. Good quality, loud sound can only be produced when the vocal cords are closely approximated. A vocal cord, paralysed in a lateral position, results in a gap during phonation, producing a weak, breathy voice. It is not usually possible to re-innervate the larynx but insertion of a prosthesis to push the paralysed cord into an optimal position for vocalizing, can allow excellent voice production. The difficulty is that, too small a prosthesis will result in a poor voice and, too large, will narrow the airway, causing breathlessness. The final decision must be a compromise between voice and airway. We believe that preoperative modelling will allow more accurate prediction of the effects of prosthesis size on both voice and airway. Although the fluid–structure interaction in this problem is important, the mechanism is normally simple. Vocal cords move up and down and laterally and medially in a systematic way and a prescribed motion may be sufficient to determine an optimal flow rate. The geometry is not as complex as that of the nasal passages although scan resolution is still an issue.

The second, increasingly common, problem is that of sleep apnoea. This has received more attention than the previous problems due to the larger numbers affected and the concern that sleep apnoea may be an important factor in some road accidents and in early death from hypertension and heart disease. However, patient-specific modelling of upper airway collapse has so far not been attempted. The major challenge in this problem is that of tackling the combination of fluid forces, structural movement and the neuromuscular activities contributing to airway collapse. Coupling passive material with fluid is difficult but neuromuscular actions make the problem even more complex. On the positive side, sleep apnoea is routinely investigated, providing high-quality digital audiovisual data during controlled sleep studies. Thus, production of a soft tissue model is possible from the experimental data.

In both problems, the unifying factor is the study of patient-specific fluid dynamics. Irrespective of other factors involved, it is essential to develop a procedure allowing repeatable fluid dynamics studies to be performed. This article is a demonstration of such a patient-specific fluid dynamics study in a human upper airway. In the present work, the fluid forces are determined, based on the modelling requirement of airway collapse. Thus, the main focus of the present study is to

DOI: 10.1002/fld

determine the pressure and, also to a lesser extent, the wall shear stress distributions in the airway, in particular at the upper and the lower oropharyngeal levels.

3. GEOMETRY RECONSTRUCTION AND MESH GENERATION

To reconstruct the geometry, an anonymous computed tomography (CT) scan from Singleton Hospital, Swansea was used. The scan was from a middle-aged woman with no known upper airway disorders. The scan resolution is 412×412 pixels and the distance between the slices is 1 mm. The scan used is shown in Figure 2. We used the commercial software, MIMICS, to extract the geometry. We show the process of interactive removal of unnecessary portions of the airway in Figure 3. The figure on the right shows the final full airway extracted from MIMICS. This geometry was extracted with a minimum of user interference. Owing to the lower resolution of the scans used, the software failed to identify the thin bony structures separating the sinuses from

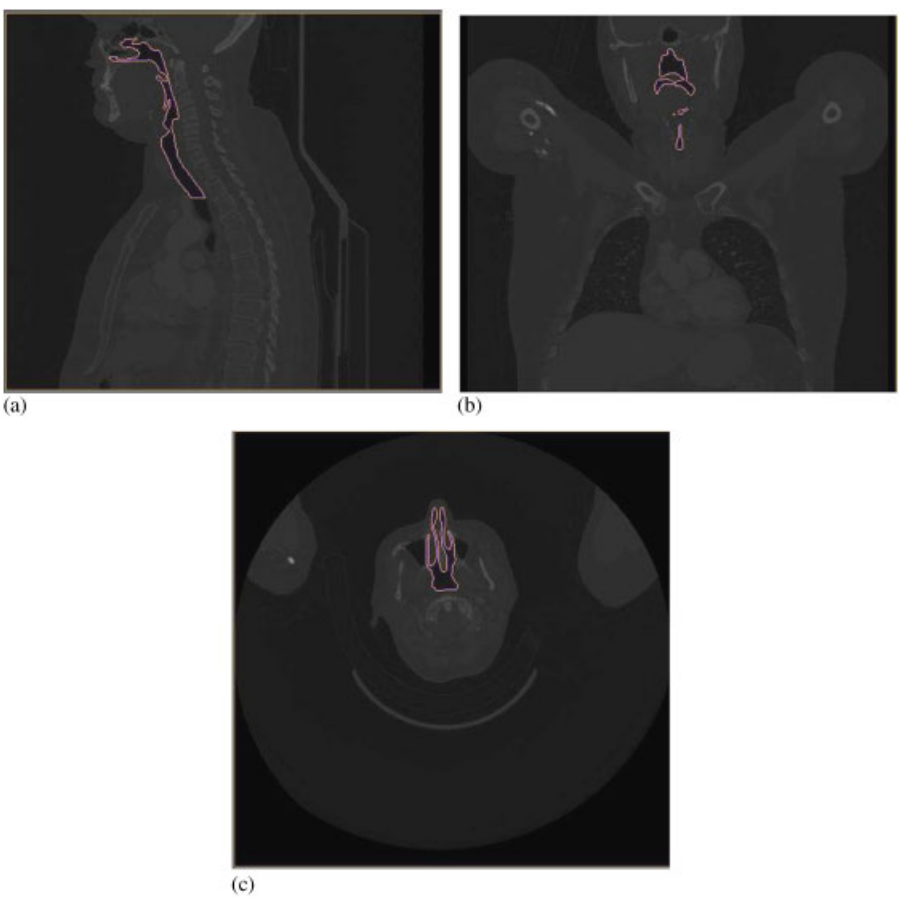

Figure 2. CT scan of a middle-aged woman: (a) side view; (b) anterior view; and (c) top view.

DOI: 10.1002/fld

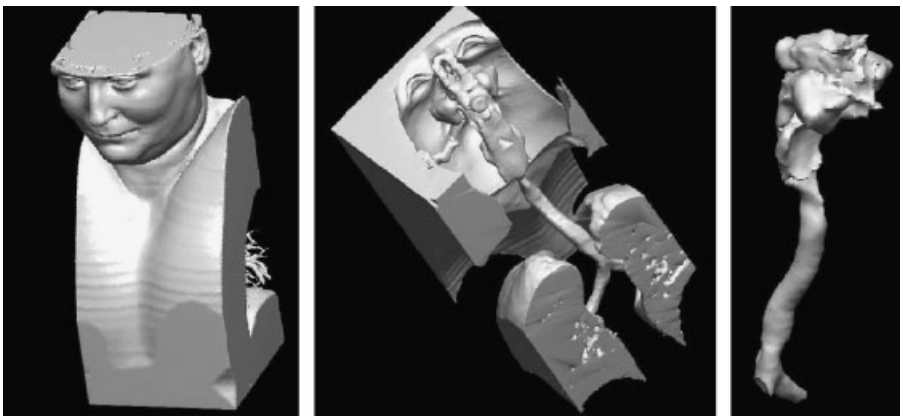

Figure 3. MIMICS reconstruction.

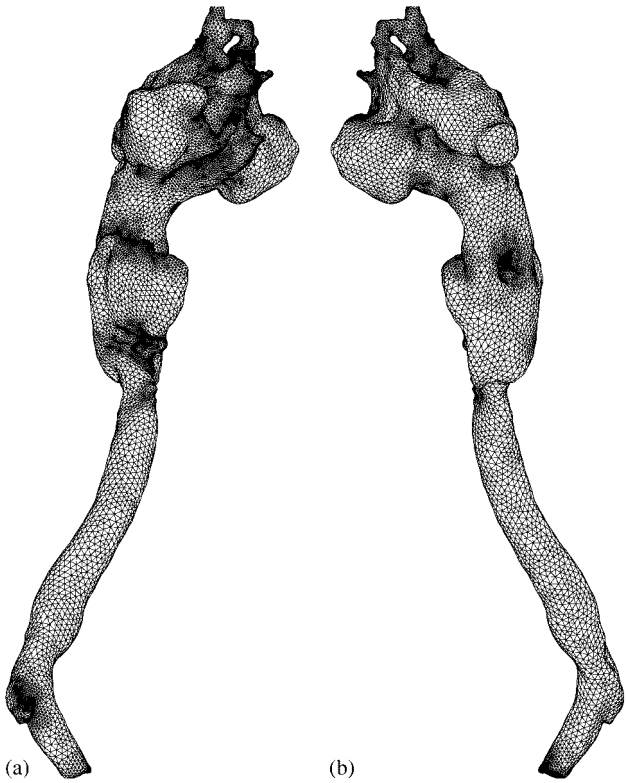

Figure 4. Initial surface mesh generated for the human upper airway:
(a) anterior view and (b) posterior view.

DOI: 10.1002/fld

the airway. As a result, the geometry included both the sinuses on the sides of the nasal passage and the ones at the forehead.

The meshing tools, including those used for surface meshing, are the ones developed at Swansea [53–55]. The STL file is converted into a surface mesh first, before generating a volume mesh. It was necessary to check for any intersecting surfaces, before the volume was generated. Views of the sample mesh generated for the full airway geometry, including the sinuses are shown in Figure 4. As seen, all the expected features of the geometry are captured.

To model the flow, we manually truncated the geometry just above the tip of the soft pallet. Although this geometry is not able to include the effects from the nasal passages, it is expected to predict the disturbance caused by larynx and vocal cords accurately. The truncated geometry was generated from a surface mesh by cutting, at a required plane, and projecting the surface points to a constant x_3 value. In this way, a smooth surface is obtained at the inlet. After meshing the cut surface with a 2D Delaunay triangulation, the volume mesh was regenerated. Figure 5 shows the truncated mesh and Figure 6 shows the surface mesh closer to the epiglottis and vocal cords. Three different meshes were generated. The mesh was progressively refined to make sure that the effect of mesh refinement on the solution is negligibly small. The first mesh consists of about 100 000 elements, the second mesh was generated with about 500 000 elements and the last

Figure 5. Reduced final, fine surface mesh: (a) anterior view and (b) posterior view.

DOI: 10.1002/fld

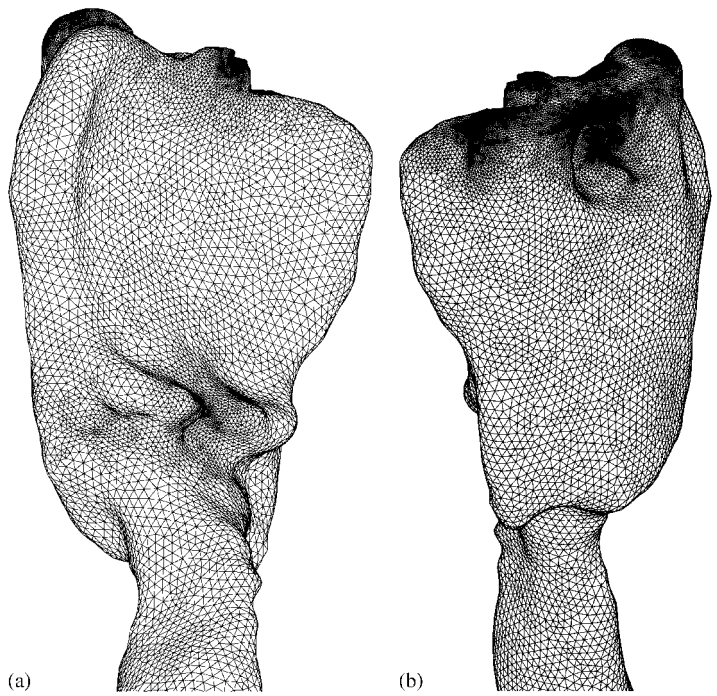

Figure 6. Reduced final, fine surface mesh: (a) anterior view and (b) posterior view.

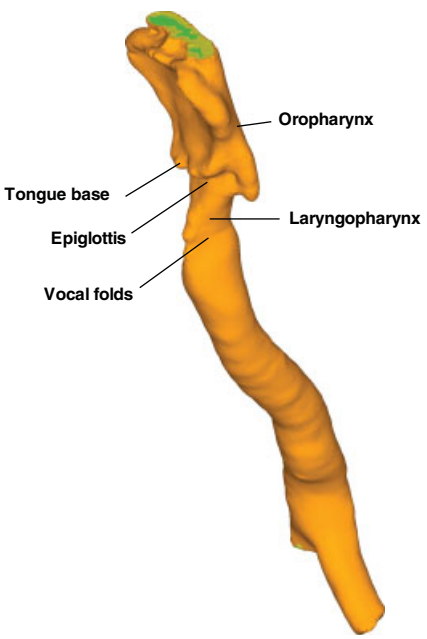

Figure 7. Final airway geometry.

DOI: 10.1002/fld

mesh contains about a million elements. Figure 7 shows the final geometry used and the details of different regions of human upper airway below tongue base.

4. GOVERNING EQUATIONS

For turbulent incompressible flow computations, the Reynolds-averaged Navier–Stokes (RANS) equations are expressed in conservation form as

Mean continuity

$$\frac{1}{\beta^2}\frac{\partial p}{\partial t}+\frac{\partial \rho \bar{u}_i}{\partial x_i}=0 \tag{1}$$

Mean momentum

$$\frac{\partial \bar{u}_i}{\partial t}+\frac{\partial}{\partial x_j}(\bar{u}_j\bar{u}_k)=-\frac{1}{\rho}\frac{\partial p}{\partial x_i}+\frac{\partial \tau_{ij}}{\partial x_j}+\frac{\partial \tau_{ij}^{\mathrm{R}}}{\partial x_j} \tag{2}$$

where β is an artificial compressibility parameter, $\bar{u}_i$ are the mean velocity components, p is the mean pressure, ρ is the density, τ_{ij} is the mean laminar shear stress tensor given as

$$\tau_{ij}=\nu\left(\frac{\partial \bar{u}_i}{\partial x_j}+\frac{\partial \bar{u}_j}{\partial x_i}-\frac{2}{3}\frac{\partial \bar{u}_k}{\partial x_k}\delta_{ij}\right) \tag{3}$$

The Reynolds stress tensor, τ_{ij}^{R}, is introduced by Boussinesq's assumption, as

$$\tau_{ij}^{\mathrm{R}}=-\overline{u_i'u_j'}=\nu_{\mathrm{T}}\left(\frac{\partial \bar{u}_i}{\partial x_j}+\frac{\partial \bar{u}_j}{\partial x_i}-\frac{2}{3}\frac{\partial \bar{u}_k}{\partial x_k}\delta_{ij}\right) \tag{4}$$

In these equations, ν is the kinematic viscosity of the fluid, ν_{T} is the turbulent eddy viscosity and δ_{ij} is the Kronecker delta.

The SA [56] model was first introduced for aerospace applications and now it is commonly used in incompressible flow calculations. The SA model is a one-equation model, which employs a single scalar equation and several constants, to model turbulence. We find this model both to be fast and accurate for incompressible and internal flows compared with other RANS models [29, 57]. The scalar equation is

$$\frac{\partial \hat{\nu}}{\partial t}+\frac{\partial u_j\hat{\nu}}{\partial x_j}=c_{b1}\hat{S}\hat{\nu}+\frac{1}{\sigma}\left[\frac{\partial}{\partial x_i}(\nu+\hat{\nu})\frac{\partial \hat{\nu}}{\partial x_i}+c_{b2}\left(\frac{\partial \hat{\nu}}{\partial x_i}\right)^2\right]-c_{w1}f_w\left[\frac{\hat{\nu}}{y}\right]^2 \tag{5}$$

where

$$\hat{S}=S+(\hat{\nu}/k^2y^2)f_{v2} \tag{6}$$

$$f_{v2}=1-X/(1+Xf_{v1}) \tag{7}$$

In Equation (6), S is the magnitude of vorticity. The eddy viscosity is calculated as

$$\nu_{\mathrm{T}}=\hat{\nu}f_{v1} \tag{8}$$

DOI: 10.1002/fld

where

$$f_{v1} = X^3/(X^3 + c_{v1}^3) \tag{9}$$

$$X = \hat{v}/v \tag{10}$$

The parameter f_w is given as

$$f_w = g\left[\frac{1+c_{w3}^6}{g^6+c_{w3}^3}\right]^{1/6} \tag{11}$$

$$g = r + c_{w2}(r^6 - r) \tag{12}$$

$$r = \frac{\hat{v}}{\hat{S}k^2y^2} \tag{13}$$

The constants are $c_{b1}=0.1355, \sigma=2/3, c_{b2}=0.622, k=0.41, c_{w1}=c_{b1}/k^2+(1+c_{b2})/\sigma, c_{w2}=0.3, c_{w3}=2$ and $c_{v1}=7.1$.

4.1. Boundary conditions

The velocity boundary conditions at the inlet were enforced based on the flow rate studied. Usual no-slip boundary conditions were assumed on the solid walls. A very small value of the turbulence parameter $\hat{v}$ was prescribed at the inlet. The value of this parameter was assumed to be zero on the walls. During the calculations, the difference between the mass flow rate at the inlet and exit was monitored and reduced to a value well below 5%. As the scheme used is explicit, the pressure at the exit is automatically maintained at zero (initial condition).

5. FLUID DYNAMICS

The CFD algorithm used here has been tested in the past for various laminar and turbulent flows. The method is based on the CBS algorithm [29–64]. The algorithm is based on the fractional step method to stabilize pressure and a characteristic-based approach to stabilize discrete convection operators. This combination, along with a local time stepping, was found to be robust [58, 59]. The method has been employed, both in its fully explicit and semi-implicit forms, in the past. We have used the artificial compressibility-based method here [60, 61]. The method solves the incompressible Navier–Stokes equations in three steps. In the first step, an intermediate momentum field is solved. In the second step, pressure is computed and in the third step, the momentum field is corrected. The one-equation SA [56, 65] turbulence model is added as a fourth step. The first three steps of the CBS scheme used in its semi-discrete form may be summarized as

Step 1: *Intermediate momentum*

$$\Delta\tilde{U}_i = \tilde{U}_i - U_i^n = \Delta t\left[-\frac{\partial}{\partial x_j}(u_jU_i) + \frac{\partial\tau_{ij}}{\partial x_j} + \frac{\partial\tau_{ij}^{\mathrm{R}}}{\partial x_j} + \frac{\Delta t}{2}u_k\frac{\partial}{\partial x_k}\left(\frac{\partial}{\partial x_j}(u_jU_i)\right)\right]^n \tag{14}$$

where $U_i^n = U_i(t_n)$; $\Delta t = t^{n+1} - t^n$ and ˜ indicates an intermediate quantity. The higher-order terms are due to time discretization using the characteristic Galerkin approach [64, 66, 67].

DOI: 10.1002/fld

Step 2: *Pressure*

$$\left(\frac{1}{\beta^2}\right)^n \Delta p = \left(\frac{1}{\beta^2}\right)^n (p^{n+1} - p^n)$$
$$= -\Delta t \left[\frac{\partial U_i^n}{\partial x_i} + \theta_1 \frac{\partial \Delta \tilde{U}_i}{\partial x_i} - \Delta t \theta_1 \left(\frac{\partial^2 p^n}{\partial x_i \partial x_i} + \theta_2 \frac{\partial^2 \Delta p}{\partial x_i \partial x_i} \right) \right] \tag{15}$$

Step 3: *Momentum correction*

$$\Delta U_i = U_i^{n+1} - U_i^n = \Delta \tilde{U}_i - \Delta t \frac{\partial p}{\partial x_i}^{n+\theta_2} \tag{16}$$

where $0.5 \leqslant \theta_1 \leqslant 1$ and $0 \leqslant \theta_2 \leqslant 1$. For the explicit scheme, employed in this study, $\theta_2 = 0$. The equations are derived from the observation that the time discretization is carried out along the characteristic. A simple approximate backward integration gives the equations with some extra convection stabilization terms (last term in the right-hand side at Step 1). These extra terms are consistent and reduce oscillations, due to the standard Galerkin discretization of convective terms. These higher-order terms are very important when the time discretization is explicit. The artificial compressibility parameter β is defined locally, based on the local velocity scales. Further details on the selection of β may be found in [60].

The scalar transport turbulence equations are also subjected to the characteristic time discretization, similar to Step 1. Once the semi-discrete form is available, the standard Galerkin spatial discretization follows [64, 67].

5.1. A model human airway problem

A model human upper airway is considered first to verify the steady-state calculations. The geometry used is an idealized oropharynx from Reference [68]. This reference provides some experimental data for the idealized geometry. Although identical reproduction of the experimental configuration is difficult, we have reproduced an approximate configuration from the geometrical data given in Heenan *et al.* [68]. We have generated an unstructured mesh with about one million tetrahedral elements to discretize the domain as shown in Figure 8.

Figures 9 and 10 show some sample qualitative results at a flow rate of 37.35 l/m. The u_3 velocity distribution clearly shows the acceleration as the flow enters the pharynx and also when it leaves the pharynx through the epiglottis. As a result of the complex nature of the geometry, some slow moving, recirculatory regions are also noted, near the entrance to pharynx. It is also observed that the majority of the pressure drop occurs as the fluid enters the pharynx and also as it passes the epiglottis. The oral cavity shows almost no pressure change. The qualitative results obtained compare well with the experimental results given by Heenan *et al.* [68].

To further increase the confidence in the flow solver, the pressure drop calculations were carried out for different flow rates. The pressure drop is calculated as the difference between the average pressure values at the inlet and exit. Figure 11 shows the comparison of pressure drop values obtained from the present numerical study and the experimental data. As seen the agreement between the two results is good. The small difference between the results may be attributed to

DOI: 10.1002/fld

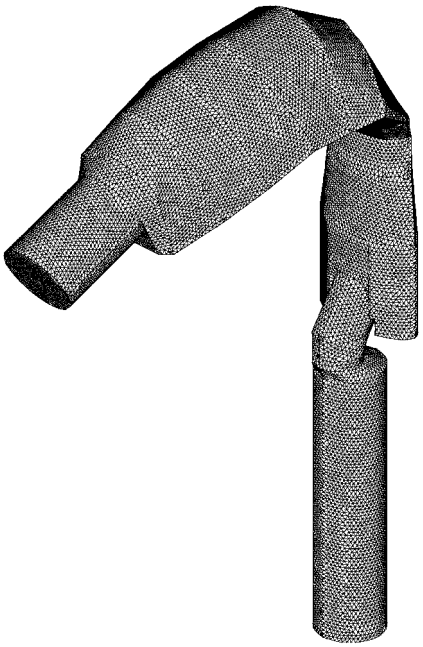

Figure 8. An idealized human upper airway model. Unstructured mesh.

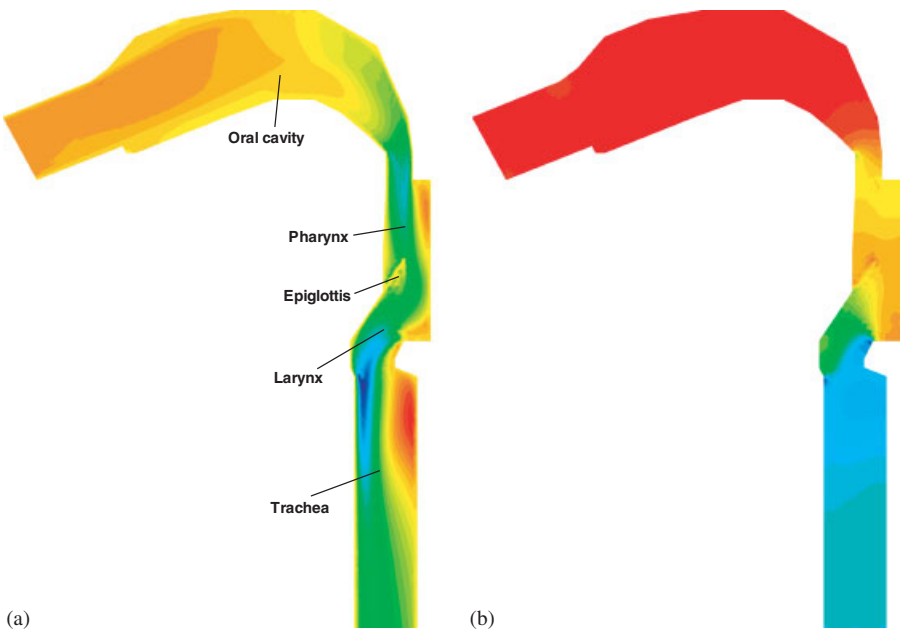

Figure 9. Flow through an idealized human upper airway, flow rate = 37.35 l/min: (a) u_3 velocity component and (b) pressure.

DOI: 10.1002/fld

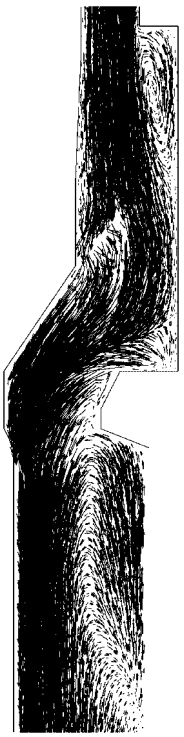

Figure 10. Flow through an idealized human upper airway. Velocity vectors.

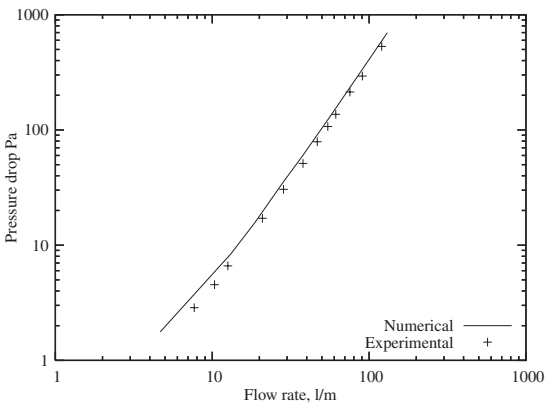

Figure 11. Flow through an idealized human upper airway. Pressure drop. Experimental data from Heenan *et al.* [68].

the minor differences in the geometry. The geometry used here was constructed from the 13 cross sections provided by Heenan *et al.* [68]. The sections were linearly connected to obtain the full geometry.

DOI: 10.1002/fld

5.2. Inhalation studies

Inhalation studies are important for determining the flow behaviour during drug deliveries. The area at the inlet of the patient-specific geometry is approximately 222 mm^2. The properties of air are assumed to be constant. A kinematic viscosity of 1.69×10^{-5} m^2/s and density of 1.2 kg/m^3 were used in the calculations. The flow rate in the human airways normally varies between 15 and 45 l/m depending on the state of the subject. The inhalation flow is studied by prescribing a velocity based on the assumed flow rate. In order to accurately represent the velocity boundary conditions, it may be essential to consider the flow through the nasal passages. As mentioned previously, it was not easy to construct the geometry of the nasal passages using low-resolution scans. We will consider the influence of nasal air passages in a future article.

The mesh used consists of about half a million elements. The mesh sensitivity study shows that, at a Reynolds number (based on 100 mm) of 15 000, there is a difference in the pressure drop of about 2.5% between meshes with half and one million linear tetrahedral elements. To obtain as accurate results as possible, we have employed one million element mesh throughout the study. At the inlet of the geometry, a constant velocity value is assumed depending on the flow rate.

The qualitative results, at an inhalation flow rate of 33.76 l/m, are presented in Figures 12–14. The vector plots in Figure 12 clearly show a recirculation region just below the vocal cords. Although the geometry looks fairly straight, the recirculation makes the physics more interesting. As expected, the flow accelerates near the tongue base (oropharynx) as it passes into the laryngopharynx (see Figure 12). The flow stabilizes and reaches a nearly developed state as it moves towards the bifurcation, within the trachea.

(a) (b)

Figure 12. Velocity vector plots at an inhaling flow rate of 33.76 l/m: (a) vectors and (b) recirculation below the vocal cords.

DOI: 10.1002/fld

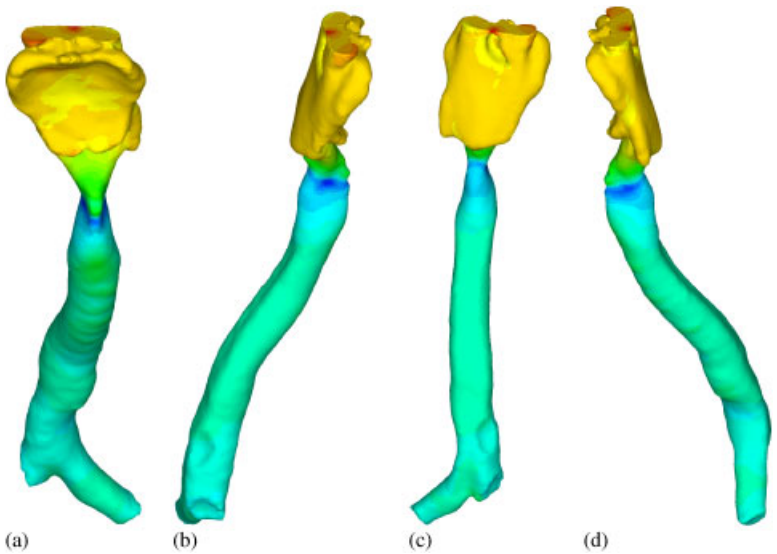

Figure 13. Pressure distribution at a flow rate of 33.76 l/min. Maximum pressure = 72.85 Pa, minimum pressure = −33.11 Pa, total pressure drop = 40.47 Pa: (a) pressure, anterior view; (b), (d) pressure, side view; and (c) pressure, posterior view.

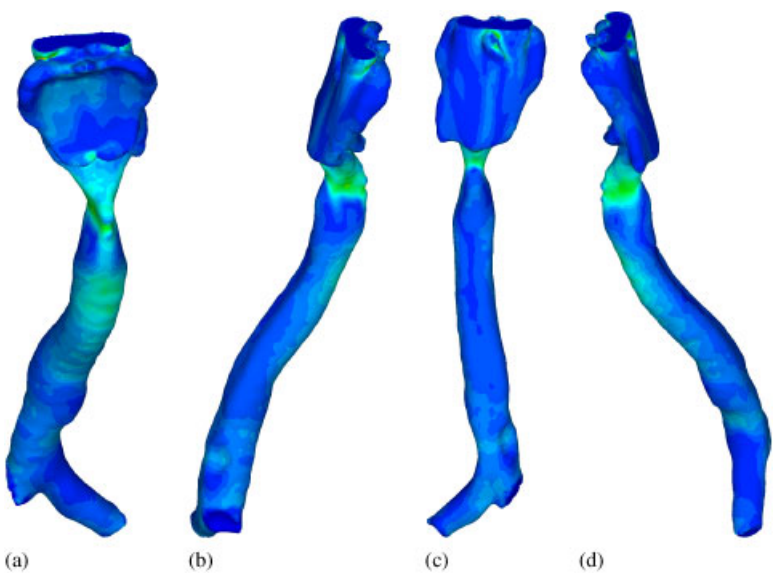

Figure 14. Wall shear stress distribution at a flow rate of 33.76 l/min. Maximum shear stress = 0.9773 Pa: (a) shear stress, anterior view; (b), (d) shear stress, side view; and (c) shear stress, posterior view.

DOI: 10.1002/fld

Figure 13 shows the pressure distribution. Once again all the action takes place near the laryngopharynx. The flow recirculation below the epiglottis also creates a negative wall pressure distribution at the posterior surface of the airway. However, the pressure at the anterior remains positive. The negative pressure created by the recirculation and the naturally narrow portion of oropharynx are responsible for the large pressure drop. As in the model airway discussed in the previous section, here also the pressure changes are almost nil in the oral cavity.

The wall shear stress distribution in Figure 14 also shows a trend in accordance with the flow distribution. The maximum wall shear stress occurs near the narrow portion of the airway. It is also noted that the wall shear stress is low near the recirculation on the posterior surface of the airway. However, the accelerating downward velocity along the anterior wall opposite to the recirculation increases the velocity gradient and increases the wall shear stress.

Table I presents comparisons of the pressure drop for the model airway presented in the previous section and the patient-specific airway studied in this subsection for three different flow rates. Although a very close match between the two is not anticipated, the difference between the pressure drops is not extremely high. The difference is about 12.5% at 50.64 l/m, about 15.21% at 33.76 l/m

Table I. Pressure drop (Pa) comparison of numerical calculations of model and patient-specific human upper airways.

Flow rate	Model airway (this study)	Cast model [69]	Patient-specific airway (this study)
16.88	12.89	—	10.15
33.76	47.73	44.00	40.47
50.64	108.45	—	94.85

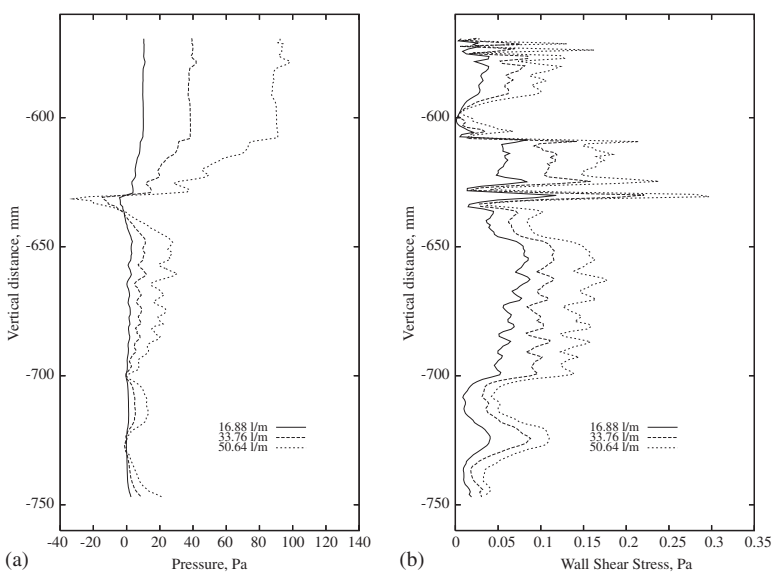

Figure 15. Pressure (a) and shear stress (b) distributions along the anterior wall up to bifurcation. The data are extracted approximately along the centre of the anterior surface.

DOI: 10.1002/fld

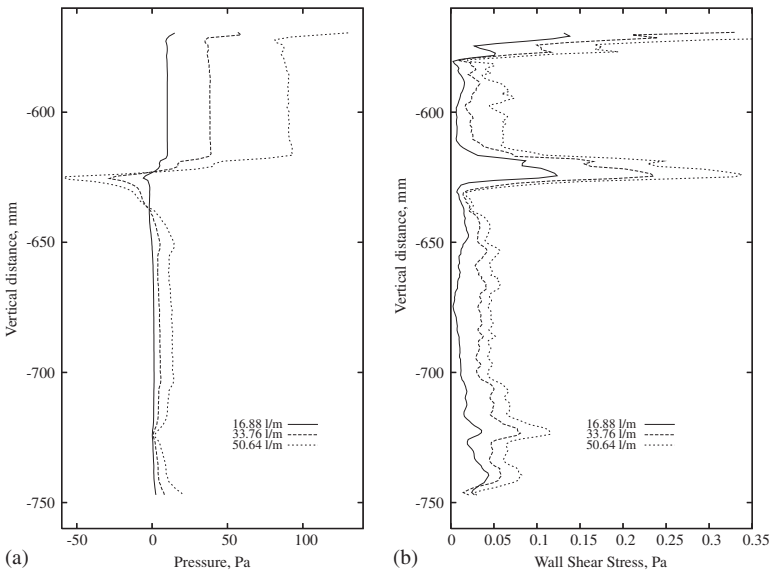

Figure 16. Pressure (a) and shear stress (b) distributions along the posterior wall up to bifurcation. The data are extracted approximately along the centre of the posterior surface.

and 21.2% at 16.88 l/m. There are two major differences between the model and patient-specific upper human airways. The first is that, although similarity exists between the two, they are not geometrically identical. The second difference is that the model airway has about a 16% longer flow path than the patient-specific airway. This second difference is clearly reflected in the higher pressure drop obtained on the model human upper airway.

Figures 15 and 16 show the wall pressure and shear stress distributions along the anterior and posterior walls of the airway up to the bifurcation. From the pressure distribution, it is clear that the major pressure drop occurs between -620 and -632 mm with the minimum pressure reported near -631 mm. This is the location just above the vocal folds in the laryngopharynx. The negative pressure difference obtained at 16.88 l/m is almost nil and, as the flow rate increases, the pressure drop noted in the laryngopharynx also increases. The negative pressure created near the vocal folds triggers a flow recirculation near the posterior surface, as the flow leaves the laryngopharynx, into the larynx and trachea. The recirculation near the posterior wall results in flow acceleration near the anterior wall, with an increase in velocity gradients along the anterior wall. This is clearly represented by the higher wall shear stress distribution on the anterior wall between -650 and -700 mm. In addition, the shear stress peaks at both the anterior and posterior walls coincide with the negative peak pressure value. The combination of the negative pressure difference and the peak shear stress value makes the laryngopharynx location an important area for airway collapse investigation. It is noted that both the pressure difference and wall shear stress distributions are not very smooth. This is mainly due to the rapid changes in the surface contours. A higher mesh resolution may marginally increase the smoothness of the wall shear stress distribution. Even on structured meshes, the shear stress distribution is expected to have rapid changes all along the surface [36].

DOI: 10.1002/fld

6. SOME DIFFICULTIES

One of the areas where we need more work is image processing to represent the geometry with a better accuracy. Generally, the amount of radiation used in a CT scan determines the image resolution. It is unethical to subject patients to higher doses of radiation. In addition to producing lower resolution, magnetic resonance-type imaging can be subjected to sensitivity factors, such as patient motion. Some of the imaging techniques are also highly invasive and involve severe side effects (e.g. 3D angiography). Thus, for the time being, to make better use of the low-resolution images, a significant amount of research needs to be focused to find better ways of reducing image noise.

The explicit fractional step method used in this study has proved to be robust for standard engineering problems but, in the present study, to conserve mass required long computational times. The implicit procedures could reduce the time needed to conserve mass. The patient-specific nature of the problems and the time taken to solve each individual problem are also likely to have an impact on the future research.

7. CONCLUSIONS

The objective of this article was to demonstrate a patient-specific fluid dynamic study in a human upper airway. Attention was focused to study the effect of steady, inhalation flow in the pharynx. The flow in the model airway studied gave a great deal of confidence in the results obtained. The patient-specific study has shown that the pressure drop is large close to the narrow portion just below the oropharynx. It has also shown that the wall shear stress is very large near the narrow portion of the pharynx. All this clearly indicate that the oropharynx and laryngopharynx are the two major areas of interest for developing an appropriate fluid-structure model for airway collapse (sleep apnoea). We are aware of the fact that to precisely model the flow, we should include the nasal passage into the model. We should also study the time-dependent breathing cycle. In addition to the above two inclusions, we may also need to account for the small change in the geometry during quite breathing. This last point may be neglected, as the small changes during quite breathing may not influence the flow field as much as the first two aspects.

In addition to the issue of creating a nasal passage geometry, the transient breathing cycle also needs to include appropriate periodic boundary conditions and turbulence at higher Reynolds numbers. While recognizing the fact that LES is probably both an affordable and accurate way for modelling turbulence in the human airway, it may be extremely difficult to satisfy meshing needs close to the solid walls of the geometry. Other options of using unsteady RANS and DES could also be exploited.

ACKNOWLEDGEMENTS

This work is fully funded by EPSRC via an Advanced Fellowship number EP/D070554. The first author also acknowledges the support of Dr Rhodri Evans of Singleton Hospital, Swansea who provided the CT scan used in this work; Mr Peter Evans of Morriston Hospital, Swansea for providing expertise to extract geometry using MIMICS and Ms Alex Arnold, a PhD student for helping with the generation of the model human upper airway geometry and mesh.

DOI: 10.1002/fld

REFERENCES

1. Taylor CA, Hughes TJR, Zarins CK. Finite element modeling of blood flow in arteries. *Computer Methods in Applied Mechanics and Engineering* 1998; **158**:155–196.
2. Calamante F, Yim PJ, Cebral JR. Estimation of bolus dispersion effects in perfusion MRI using image-based computational fluid dynamics. *NeuroImage* 2003; **19**:341–353.
3. Castro MA, Putman CM, Cebral JR. Patient-specific computational modeling of cerebral aneurysms with multiple avenues of flow from 3d rotational angiography images. *Academic Radiology* 2006; **13**:811–821.
4. Cebral JR, Yim PJ, Löhner R, Sato O, Choyke PL. Blood flow modeling in carotis arteries with computational fluid dynamics and MR imaging. *Academic Radiology* 2002; **9**:1286–1299.
5. Kaazempur-Mofrad MR, Bathe M, Karcher H, Younis HF, Seong HC, Shim EB, Chan RC, Hinton DP, Isasi AG, Upadhyaya A, Powers MJ, Griffiths LG, Kamm RD. Role of simulation in understanding biological systems. *Computers and Structures* 2003; **81**:715–726.
6. Löhner R, Cebral J, Soto O, Yim P, Burgess JE. Applications of patient-specific CFD in medicine and life sciences. *International Journal for Numerical Methods in Fluids* 2003; **43**:637–650.
7. Milner JS, Moore JA, Rutt BK, Steinman DA. Hemodynamics of human carotid artery bifurcations: computational studies with models reconstructed from magnetic resonance imaging of normal subjects. *Journal of Vascular Surgery* 1998; **28**:143–155.
8. Moreno R, Nicoud F, Rousseau H. Non-linear-transformation field to build moving meshes for patient specific blood flow simulations. In *European Conference on Computational Fluid Dynamics*, *ECCOMAS CFD 2006*, Wesseling P, Onate E, Periaus J (eds). TU Delft: The Netherlands, 2006.
9. Steinman DA, Milner JS, Norley CJ, Lownie SP, Holdsworth DW. Image-based computational simulation of flow dynamics in a giant intracranial aneurysm. *American Journal of Neuroradiology* 2003; **24**:559–566.
10. Tabor G, Tame D, Pierron F, Young PG, Watkinson A, Thompson J. Patient specific arterial flow simulation with additional geometric elements. In *European Conference on Computational Fluid Dynamics*, *ECCOMAS CFD 2006*, Wesseling P, Onate E, Periaus J (eds). TU Delft: The Netherlands, 2006.
11. Torii R, Oshima M, Kobayashi T, Takagi K, Tezduyar TE. Computer modelling of cardiovascular fluid–structure interactions with the deforming-spatial-domain/stabilized space–time formulation. *Computer Methods in Applied Mechanics and Engineering* 2006; **195**:1885–1895.
12. Wolters BJBM, Rutten MCM, Schurink GWH, Kose U, de Hart J, van de Vosse FN. A patient-specific computational model of fluid–structure interaction in abdominal aortic aneurysms. *Medical Engineering and Physics* 2005; **27**:871–883.
13. Valencia A, Botto S, Sordo J, Galvez M, Badilla L. Comparison of haemodynamics in vertebral aneurysms of different sizes located in the opthalmic artery. *International Journal for Numerical Methods in Fluids* 2007; **53**:793–809.
14. Mynard JP, Nithiarasu P. A one dimensional arterial blood flow model incorporating ventricular pressure, aortic valve and regional coronary flow using the locally conservative Galerkin (LCG) method. *Communications in Numerical Methods in Engineering* 2008; DOI: 10.1002/cnm.1117.
15. Ebden P, Jenkins A, Houston G, Davies BH. Comparison of 2 high-dose corticosteroid aerosol treatments, beclomethasone dipropionate (150 ug day) and budesonide (1600 ug day), for chronic asthma. *Thorax* 1986; **41**:869–874.
16. Hawkins DB, Luxford WM. Laryngeal stenosis from endotracheal intubation—a review of 58 cases. *Annals of Otology*, *Rhinology and Laryngology* 1980; **89**:454–458.
17. Wright J, Johns R, Watt I, Melville A, Sheldon T. Health effects of obstructive sleep apnoea and the effectiveness of continuous positive airways pressure: a systematic review of the research evidence. *British Medical Journal* 1997; **314**:851–860.
18. Ayappa I, Rapoport DM. The upper airway in sleep: physiology of the pharynx. *Physiological Review* 2003; **7**:9–33.
19. De Boer MF, McCormick LK, Pruyn JFA, Ryckman RM, van den Borne BW. Physical and psychosocial correlates of head and neck cancer: a review of the literature. *Otolaryngology—Head and Neck Surgery* 1999; **120**:427–436.
20. Constantian MB, Clardy RB. The relative importance of septal and nasal valvular surgery in correcting airway obstruction in primary and secondary rhinoplasty. *Plastic and Reconstructive Surgery* 1996; **98**:38–54.
21. Kulish V. *Human Respiration. Anatomy and Physiology*, *Mathematical Modeling*, *Numerical Simulation and Applications*. WIT Press: Southampton, 2006.
22. Cebral JR, Summers RM. Tracheal and central bronchial aerodynamics using virtual bronchoscopy and computational fluid dynamics. *IEEE Transactions on Medical Imaging* 2004; **23**:1021–1033.

23. Takano H, Nishida N, Itoh M, Hyo N, Majima Y. Inhaled particle deposition in unsteady-state respiratory flow at a numerically constructed model of the human larynx. *Journal of Aerosol Medicine* 2006; **19**:314–328.
24. Wall W, Rabczuk T. Fluid–structure interaction in lower airways of ct-based lung geometries. *International Journal for Numerical Methods in Fluids* 2008; DOI: 10.1002/fld.1763.
25. Ma B, Lutchen KR. An anatomically based hybrid computational model of the human lung and its application to low frequency oscillatory mechanics. *Annals of Biomedical Engineering* 2006; **34**:1691–1704.
26. Jeong S-J, Kim W-S, Sung S-J. Numerical investigation on the flow characteristics and aerodynamic force of the upper airway of patient with sleep apnea using computational fluid dynamics. *Medical Engineering and Physics* 2007; **29**:637–651.
27. Brouns M, Jayaraju ST, Lacor C, De Mey J, Noppen M, Vincken W, Verbanck S. Tracheal stenosis: a flow dynamics study. *Journal of Applied Physiology* 2007; **102**:1178–1184.
28. Jayaraju ST, Brouns M, Verbanck S, Lacor C. Fluid flow and particle deposition analysis in a realistic extrathoracic airway model using unstructured grids. *Journal of Aerosol Science* 2007; **38**:494–508.
29. Nithiarasu P, Liu C-B, Massarotti N. Laminar and turbulent flow through a model human upper airway. *Communications in Numerical Methods in Engineering* 2007; **23**:1057–1069.
30. Wilquem F, Degrez G. Numerical modeling of steady inspiratory airflow through a three-generation model of the human central airways. *Journal of Biomechanical Engineering—Transactions of the ASME* 1997; **119**:59–65.
31. Martonen TB, Zhang ZQ, Yu GQ, Musante CJ. Three-dimensional computer modeling of the human upper respiratory tract. *Cell Biochemistry and Biophysics* 2001; **35**:255–261.
32. Zhao Y, Brunskill CT, Lieber BB. Inspiratory and expiratory steady flow analysis in a model symmetrically bifurcating airway. *Journal of Biomechanical Engineering—Transactions of the ASME* 1997; **119**:52–58.
33. Grotberg JB, Jensen OE. Biofluid mechanics in flexible tubes. *Annual Reviews of Fluid Mechanics* 2004; **36**:121–147.
34. Marzo A, Luo XY, Bertram CD. Three-dimensional collapse and steady flow in thick-walled flexible tubes. *Journal of Fluids and Structures* 2005; **20**:817–835.
35. Luo XY, Hinton JS, Liew TT, Tan KK. LES modelling of flow in a simple airway model. *Medical Engineering and Physics* 2004; **26**:403–413.
36. Li W-I, Perzl M, Heyder J, Langer R, Brain JD, Englmeier K-H, Niven RW, Edwards DA. Aerodynamics and aerosol particle deaggregation phenomena in model oral-pharyngeal cavities. *Journal of Aerosol Science* 1996; **27**:1269–1286.
37. Hofmann W. Modeling techniques for inhaled particle deposition: the state of the art. *Journal of Aerosol Medicine* 1996; **9**:369–388.
38. Balashazy I, Heistracher T, Hofmann W. Air flow and particle deposition patterns in bronchial airway bifurcations: the effect of different CFD models and bifurcation geometries. *Journal of Aerosol Medicine* 1996; **9**:287–301.
39. Kaufman JW, Scherer PW, Yang CCG. Predicted combustion product deposition in the human airway. *Toxicology* 1996; **115**:123–128.
40. Li W-I, Edwards DA. Aerosol particle transport and deaggregation phenomena in the mouth and throat. *Advanced Drug Delivery Reviews* 1997; **26**:41–49.
41. Gemci T, Corcoran TE, Yakut K, Shortall B, Chigier N. Spray dynamics and deposition of inhaled medications in the throat. *ILASS—Europe 2001*, Zurich, September 2–6, 2001.
42. Gemci T, Corcoran TE, Chigier N. A numerical and experimental study of spray dynamics in a simple throat model. *Aerosol Science and Technology* 2002; **36**:18–38.
43. Sheu TWH, Wang SK, Tsai SF. Finite element analysis of particle motion in steady inspiratory airflow. *Computer Methods in Applied Mechanics and Engineering* 2002; **191**:2681–2698.
44. Martonen TB, Zhang Z, Yue G, Musante CJ. 3-D particle transport within the human upper respiratory tract. *Journal of Aerosol Science* 2002; **33**:1095–1110.
45. Hofmann W, Golser R, Balashazy I. Inspiratory deposition efficiency of ultrafine particles in a human airway bifurcation model. *Aerosol Science and Technology* 2003; **37**:988–994.
46. van Ertbruggen C, Hirsch C, Paiva M. Anatomically based three-dimensional model of airways to simulate flow and particle transport using computational fluid dynamics. *Journal of Applied Physiology* 2005; **98**:970–980.
47. Nishino T, Hiraga K. Coordination of swallowing and respiration in unconscious subjects. *Journal of Applied Physiology* 1991; **70**:988–993.
48. Fouke JM, Teeter JP, Strohl KP. Pressure–volume behaviour of the upper airway. *Journal of Applied Physiology* 1986; **61**:912–918.
49. Strohl KP, Fouke JM. Dialating forces on the upper airway of anesthetized dogs. *Journal of Applied Physiology* 1985; **58**:452–458.

50. Verneuil A, Berry DA, Kreiman J, Gerratt BR, Ye M, Berke GS. Modelling measured glottal volume velocity waveforms. *Annals of Otology, Rhinology and Laryngology* 2003; **112**:120–131.
51. Brancatisano T, Collett P, Engel L. Respiratory movements of the vocal cords. *Journal of Applied Physiology* 1983; **54**:1269–1276.
52. Renotte C, Bouffioux V, Wilquem F. Numerical 3d analysis of oscillatory flow in the time-varying laryngeal channel. *Journal of Biomechanics* 2000; **33**:1637–1644.
53. Wang DS, Hassan O, Morgan K, Weatherill NP. Enhanced remeshing from STL files with applications to surface grid generation. *Communications in Numerical Methods in Engineering* 2007; **23**:227–239.
54. Wang DS, Hassan O, Morgan K, Weatherill NP. Eqsm: an efficient high quality surface grid generation method based on remeshing. *Computer Methods in Applied Mechanics and Engineering* 2006; **195**:5621–5633.
55. Wang DS, Hassan O, Morgan K, Weatherill NP. Efficient surface reconstruction from contours based on two-dimensional Delaunay triangulation. *International Journal for Numerical Methods in Engineering* 2006; **65**: 734–751.
56. Spalart PR, Allmaras SR. A one-equation turbulence model for aerodynamic flows. *AIAA Paper 92-0439*, 1992.
57. Nithiarasu P, Liu C-B. An explicit characteristic based split (CBS) scheme for incompressible turbulent flows. *Computer Methods in Applied Mechanics and Engineering* 2006; **195**:2961–2982.
58. Codina R, Owen H-C, Nithiarasu P, Liu C-B. Numerical comparison of CBS and SGS as stabilization techniques for the incompressible Navier–Stokes equations. *International Journal for Numerical Methods in Engineering* 2006; **66**:1672–1689.
59. Massarotti N, Fausto F, Lewis RW, Nithiarasu P. Explicit and semi-implicit CBS procedures for incompressible viscous flows. *International Journal for Numerical Methods in Engineering* 2006; **66**:1618–1640.
60. Nithiarasu P. An efficient artificial compressibility (AC) scheme based on the characteristic based split (CBS) method for incompressible flows. *International Journal for Numerical Methods in Fluids* 2003; **56**:1815–1845.
61. Nithiarasu P, Mathur JS, Weatherill NP, Morgan K. Three-dimensional incompressible flow calculations using the characteristic based split (CBS) scheme. *International Journal for Numerical Methods in Fluids* 2004; **44**:1207–1229.
62. Zienkiewicz OC, Codina R. A general algorithm for compressible and incompressible flow—part i. The split, characteristic based scheme. *International Journal for Numerical Methods in Fluids* 1995; **20**:869–885.
63. Zienkiewicz OC, Nithiarasu P, Codina R, Vazquez M, Ortiz P. The characteristic-based-split (CBS) procedure: an efficient and accurate algorithm for fluid problems. *International Journal for Numerical Methods in Fluids* 1999; **31**:359–392.
64. Zienkiewicz OC, Taylor RL, Nithiarasu P. *The Finite Element Method for Fluid Dynamics*. Elsevier Butterworth-Heinemann: Burlinton, MA, 2005.
65. Spalart PR, Jou WH, Strelets M, Allmaras SR. Comments on the feasibility of LES for wings, and on a hybrid RANS/LES approach. *Advances in DNS/LES*: *First AFOSR International Conference on DNS/LES*, Liu C, Liu Z (eds). Greyden: Columbus, OH, 1997.
66. Löhner R, Morgan K, Zienkiewicz OC. The solution of non-linear hyperbolic equation systems by the finite element method. *International Journal for Numerical Methods in Fluids* 1984; **4**:1043–1063.
67. Nithiarasu P, Codina R, Zienkiewicz OC. The characteristic based split (CBS) scheme—a unified approach to fluid dynamics. *International Journal for Numerical Methods in Engineering* 2006; **66**:1514–1546.
68. Heenan AF, Matida E, Pollard A, Finlay WH. Experimental measurements and computational modeling of the flow in an idealized human oropharynx. *Experiments in Fluids* 2003; **35**:70–84.
69. Kleinstreuer C, Zhang Z. Laminar-to-turbulent fluid–particle flows in a human airway model. *International Journal of Multiphase Flow* 2003; **29**:271–289.

DOI: 10.1002/fld